Dispersion and deposition of firebrands in a turbulent boundary layer

Chandana Anand, Babak Shotorban*, Shankar Mahalingam

Department of Mechanical and Aerospace Engineering, The University of Alabama in Huntsville, Huntsville, AL 35899, USA

ABSTRACT

The dispersion and deposition of cylindrical shaped firebrands of constant mass in a turbulent boundary layer was investigated by large eddy simulation of air flow, with firebrands individually tracked in a Lagrangian framework. The carried firebrands experienced both translation and rotation as gravity, drag and lift forces acted on them. Simulations were carried out in a turbulent boundary layer with a free stream wind velocity of 18.8 m/s, an initial boundary layer height of 25 m, with firebrand densities of 70, 230, and 570 kg/m³ and release heights of 20 m and 40 m. Identical firebrands were consecutively released under identical initial conditions after the turbulent flow reached a statistically stationary state. The motion and deposition locations of firebrands were characterized by tracking tens of thousands of firebrands in each simulation and computing statistical quantities such as dispersion and diffusion of flying firebrands, and the joint probability density function of the coordinates of the deposited firebrands. For all simulated cases, the distribution of deposited firebrands exhibited symmetry in the spanwise direction. The normalized mean position of the deposited firebrands in the streamwise direction increased approximately by a factor of two when the density of firebrands decreased from 570 kg/m³ to 70 kg/m³. Also, the ground distribution of firebrands that were released from a higher elevation was found more leptokurtic with a multivariate kurtosis deviating more than 5% of that of a normal distribution.

© 2018 Elsevier Ltd. All rights reserved.

1. Introduction

Spotting, which is the creation of a secondary (spot) fire by flying firebrands (also referred to as embers) that originate from a primary fire, is a common mechanism for the spread of wildland and wildland-urban interface (WUI) fires (Albini, 1979; Koo et al., 2010). Firebrands are burning or glowing fragments of vegetation such as twigs, barks, leaves and in WUI areas, wood shakes and shingles. Many studies were performed to understand the spotting mechanism and the role of firebrands in the spread of fires (see review articles by Koo et al. (2010) and Fernandez-Pello (2017)).

Firebrands are lofted by flames, plumes, convection columns and fire whirls of primary fires, and depending on the wind conditions, they are carried over a distance ranging from a few meters to tens of kilometers (Fryer and Johnson, 1988). According to the distance traversed by the firebrands, spotting can be classified as short-range (few tens of meters), intermediate-range, and long-range (tens of kilometers) (Albini, 1983). In particular, the intermediate/long range spotting is known to cause destruction of residential structures in WUI regions prior to the arrival of the main fire front (Maranghides and Mell, 2011). The motion of a firebrand from

release to landing can be thought of as undergoing three sequential stages: lofting, propagation, and landing, as shown in Fig. 1. The firebrand conditions such as mass, size and geometrical shape are important to the firebrand motion in all these stages. So are the ambient conditions, which can drastically change from one stage to another. For instance, in the lofting stage, it is the convective columns of the primary fire responsible for the predominantly upward motion and lofting of firebrands.

The propagation stage may be considered lacking for short-range spotting whereas it can constitute a long section of the overall distance a firebrand travels in long-range spotting. The ambient wind conditions play a significant role in how firebrands are carried in this stage. As the firebrand is carried downward, the impact of flow alteration induced by the primary fire becomes less significant on the firebrand. Hence, firebrands that are sufficiently away from the primary fire are mainly carried by the ambient wind in regions nearly devoid of any direct fire influence. In the landing stage, the firebrands descend and depending on their thermal energy content and ignitability condition of the recipient fuel, they may create spot fires after settling.

Several previous works are relevant to the present study. Tarifa et al. (1965) performed wind tunnel experiments with spherical and cylindrical tethered firebrands of various sizes and material properties. From these experiments, they found correlations for drag and determined the paths followed by firebrands numeri-
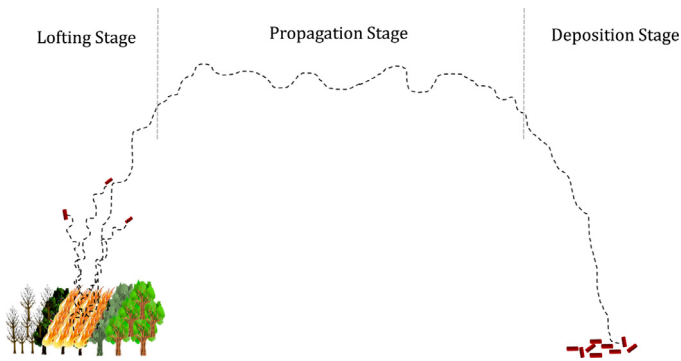
Fig. 1. Schematic diagram of the three stages of firebrand transport (a) lofting, (b) propagation and (c) deposition.

cally. In the numerical calculations, they made two critical assumptions: firebrands fall at their terminal velocities and the horizontal component of the firebrand velocity to asymptote towards the horizontal component of background fluid velocity. Stephen and Fernandez-Pello (1998) and Anthenien et al. (2006) simulated transport of firebrands in an atmospheric boundary layer modeled by a prescribed horizontal velocity, which varied with elevation according to the logarithmic or power law correlation. Furthermore, they assumed firebrands to be spherical in shape and influenced by drag and gravity forces.

Cylinders are the most common shapes for firebrands generated in wildfires (Manzello et al., 2007; 2008). In more recent works, firebrands were assumed cylindrical and/or disk-shaped under the action of the forces of drag, lift and gravity (Himoto and Tanaka, 2005; Sardoy et al., 2007; 2008; Koo et al., 2012; Oliveira et al., 2014).

The transport of firebrands lofted by buoyant plumes representing wildfires in cross flows has been the subject of previous computational fluid dynamics (CFD) based works. Sardoy et al. (2007, 2008), Huang et al. (2007) and Koo et al. (2012) described the background flow by the Reynolds averaged Navier-Stokes (RANS) equations and used the obtained mean flow velocities to advance firebrands. However, in these works the explicit role of turbulent fluctuations on the motion of firebrands was neglected. A precise description of turbulent dispersion/ diffusion of firebrands requires a full resolution of these fluctuations.

Himoto and Tanaka (2005), Pereira et al. (2015), Thurston et al. (2017) and Tohidi and Kaye (2017b) conducted large-eddy simulation (LES) to model the background flow field. In LES, resolved velocities are used to advance firebrands so the turbulent fluctuation effects on firebrands are directly taken into account to a great extent. Only the effects of the subgrid scales, which contain significantly less turbulent kinetic energy than the resolved scales, are discarded on firebrands.

Himoto and Tanaka (2005) considered disk-shaped firebrands under the drag, lift, and gravitational forces and released them from a point very close to the ground over a heat source representing a primary fire and found that the distribution of landed firebrands exhibited a log-normal function in the streamwise direction and a normal distribution in the spanwise direction. Pereira et al. (2015) treated firebrands as spherical particles under drag and gravitational forces. Thurston et al. (2017) completely neglected the firebrand inertia, assuming the firebrand velocity is the sum of the still-fluid terminal velocity and the resolved velocity of the background flow. This neglect is valid only for firebrands with very small masses (Maxey, 1987). Tohidi and Kaye (2017b) conducted LES for their laboratory experimental configuration (Tohidi and Kaye, 2017a) where non-burning firebrands were released in a combined field of two canonical wall-bounded flows: a fully developed channel flow and a fully developed pipe flow. In this configuration, firebrands were mainly lofted by the updraft of the fully developed pipe flow and transported downwind by the combined flow field. The firebrand paths for varying lengths were then statistically characterized as a function of the downwind distance. Here, the interaction of these flows somewhat resembled the cross-flow condition in a wildfire event; however, this interaction did not not account for the non-isothermal buoyancy effects. Other relevant works on particle-laden flows characterizing the transport of spherical particles in spatially developing turbulent boundary layers and channel flows are further described in Sardina et al. (2012, 2014), Pitton et al. (2012) and Chernogorova and Vulkov (2014). Sardina et al. (2014) emphasized that rigid spherical particles exhibit slower diffusion in the outer region of the turbulent boundary layer and an enhanced turbophoretic drift in the inner region close to the wall.

In the present work, firebrands carried by wind are studied in a turbulent boundary layer simulated by LES. Our main objective is to understand the turbulent dispersion of firebrands and its subsequent effects on the ground distribution of deposited firebrands. The study is arguably most relevant to the landing stage of firebrands for intermediate or long-range spotting, as the primary fire or its influence on the carrier flow is not included in the simulations.

2. Mathematical and computational approaches

2.1. LES of turbulent boundary layer

The Wildland-urban interface Fire Dynamics Simulator (WFDS) (Mell et al., 2009; McGrattan et al., 2013), as set up to use the dynamic Smagorinsky model for the subgrid-scale stresses for LES, is employed in this study. Although the dynamic Smagorinsky model has the advantage that the model coefficient for the eddy viscosity is dynamically calculated based on the local flow conditions, it requires additional computational time. For the results described in this paper, heat transfer or combustion processes were not considered, hence the features that model the transport of energy and chemical species in WFDS were not utilized. Since the relevant governing equations are standard and described comprehensively in the references cited, they are not described here.

A three dimensional rectangular domain with the specifics illustrated in Section 3 was used in the simulations. At the top boundary, $\partial u/\partial z = \partial v/\partial z = 0$ and $w = U_\infty d\delta^*/dx$, where x, y and z are the coordinates in the streamwise, spanwise and vertical direction and u, v and w are the associated resolved velocity components respectively. Here, U_∞ is the mean free stream velocity, and $\delta^*(x)$ is the displacement thickness. Since turbulence is assumed to be spatially homogeneous in the spanwise direction, a periodic boundary condition is imposed on the lateral sides of the domain. At the exit boundary, a convective outflow boundary condition (Orlanski, 1976; Mahalingam et al., 1990) was implemented and added as a new feature to WFDS. This condition is imposed by $\partial u_i/\partial t + c\partial u_i/\partial x = 0$, where the convective speed c is adjusted to ensure that global mass conservation is satisfied. Here, subscript $i \equiv 1,2,3$ indicates the components of the vector in streamwise, spanwise and vertical directions, respectively. The convective outflow boundary condition is well suited for the problem discussed in this paper wherein the velocity component perpendicular to the outflow plane is significant. To handle this boundary condition, a first order upwind differencing scheme was used to discretize the spatial derivative and the second order explicit predictor corrector scheme was used to discretize the temporal derivative which is in accordance with the temporal discretization used in WFDS.

To generate the turbulent boundary layer, the recycling method proposed by Lund et al. (1998) was used in this study and added as

a new feature to WFDS. According to this method, velocity components at a downstream location are rescaled and recycled to generate a turbulent boundary layer. The premise behind this approach is the inherent similarity in the mean and turbulence properties exhibited by turbulent boundary layers. The velocity components in the inner and outer layer of the boundary layer at a recycling plane are decomposed as, $u_i = \bar{u}_i + u_i''$, where $\bar{u}_i$ and u_i'' are the mean and fluctuating components, respectively. The overbar indicates averaging over time and space in spanwise direction. Since the velocity profile satisfies scale similarity within the boundary layer, a scaling factor based on friction velocity is used to rescale the mean and fluctuating components. To apply the recycling procedure, first the turbulent boundary layer is divided into inner and outer regions. In the inner region where viscous effects are predominant, the law of the wall is used to relate the velocity components at the recycling plane to that of the inlet plane. Similarly, away from the wall, in the outer region, the law of the wake (Coles, 1956) is used. Accordingly, the composite profile over the entire boundary layer is represented by

$$u_{i,\text{inlet}} = \left[\bar{u}_{i,\text{inlet}} + u_{i,\text{inlet}}''\right]^{\text{inner}} [1 - W]$$
$$+ \left[\bar{u}_{i,\text{inlet}} + u_{i,\text{inlet}}''\right]^{\text{outer}} W, \tag{1}$$

where W is a weighting function which takes into account the transition from inner to outer layer (Lund et al., 1998). In the current work, the boundary layer was simulated for two Reynolds number cases, i.e., $\text{Re}_\theta = 10^3$ and 10^6, as illustrated in Section 4. Here, Re_θ is defined based on the momentum thickness at the inlet and the freestream velocity (Lund et al., 1998). The viscous layer was resolved at the wall for the low Reynolds number case whereas the Werner-Wengle wall model (Werner and Wengle, 1993) was used for the high Reynolds number case with the first off-wall grid point lying in the logarithmic region of the turbulent boundary layer.

2.2. Firebrand motion

A module was developed within the WFDS framework to solve the translational and rotational motion of cylindrical firebrands. These motions are described in the Lagrangian framework through solving a set of equations that are presented here for an individual firebrand (Yin et al., 2003; Oliveira et al., 2014). The firebrands are treated as point particles and the impact of SGS on them is neglected. Heavier firebrands are expected to be less sensitive to subgrid scale fluctuations. There are previous models based on deterministic approaches, e.g., Shotorban and Mashayek (2005), or stochastic approaches, e.g., Shotorban and Mashayek (2006), to take the effects of these fluctuations into account for spherical particles experiencing the drag force. The extension of these models to include cylindrical particles is not trivial and beyond the scope of the current study.

Fig. 2 shows a schematic diagram with the forces acting on a cylindrical firebrand carried in a flow. If $\vec{x}_p(t)$ and $\vec{V}_p(t)$ denote the position and velocity of the center of mass, then

$$\frac{d\vec{x}_p}{dt} = \vec{V}_p, \tag{2}$$

$$m_p \frac{d\vec{V}_p}{dt} = \vec{F}_G + \vec{F}_D + \vec{F}_L, \tag{3}$$

where m_p is the firebrand mass and $\vec{F}_G$, $\vec{F}_D$, and $\vec{F}_L$ are the gravitational, drag, and lift forces, respectively. Here $\vec{F}_G$, which includes the buoyancy effect, is given by:

$$\vec{F}_G = (\rho_p - \rho_{\text{gas}})\forall_p \vec{g}, \tag{4}$$

where ρ_p and ρ_{gas} denote the density of the firebrand and the carrier flow, respectively, $\forall_p$ is the firebrand volume, and $\vec{g}$ is
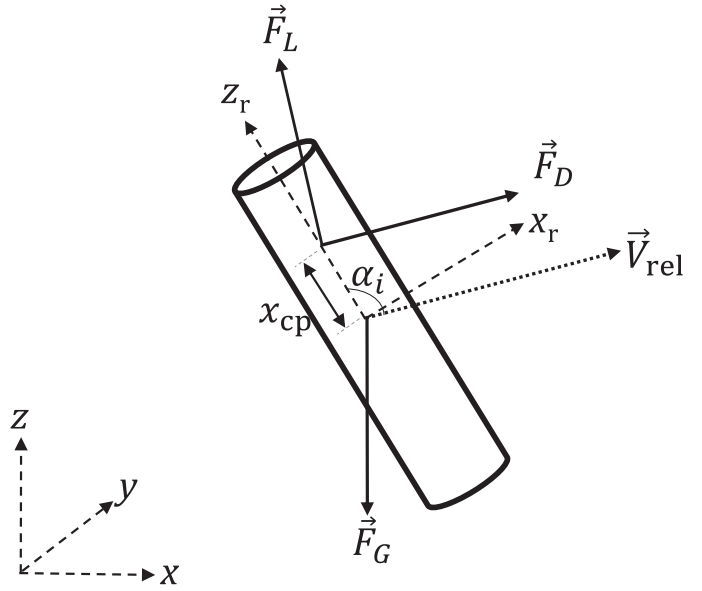

Fig. 2. Schematic diagram of a cylinder in a cross flow with the inertial and rotating coordinate systems, and acting forces.

the gravitational acceleration. In Eq. (3), $\vec{F}_D$ and $\vec{F}_L$ are calculated through a model proposed by Hoerner (1965) for cylindrical objects:

$$\vec{F}_D = 2C_D \rho_{\text{gas}} ab|V_{\text{rel}}||\sin\alpha|^3 \vec{V}_{\text{rel}}, \tag{5}$$

$$\vec{F}_L = 2C_D \rho_{\text{gas}} ab(|V_{\text{rel}}|\sin\alpha)^2 \cos\alpha \frac{\hat{z}_r \times \vec{V}_{\text{rel}} \times \vec{V}_{\text{rel}}}{|\hat{z}_r \times \vec{V}_{\text{rel}} \times \vec{V}_{\text{rel}}|}, \tag{6}$$

where a and b denote the radius and length of the cylinder, respectively, $\vec{V}_{\text{rel}}(t) = \vec{u}(\vec{x}_p(t), t) - \vec{V}_p(t)$ is the cylinder velocity relative to the local flow, where $\vec{u}(\vec{x}, t)$ is the resolved Eulerian velocity of the fluid flow. The model proposed by Hoerner (1965) was based on experiments performed on cylindrical objects, wires and cables subjected to cross-flow scenarios. This model is more suitable for cylindrical objects subjected to flows with sub-critical Reynolds numbers, $\text{Re}_b < 10^5$. It is noted that the Hoerner's assumption serves as a limitation in determining the drag coefficient in the event of flow separation and generation of wake behind cylindrical objects. In computations, $\vec{u}(\vec{x}_p(t), t)$ is calculated via a trilinear interpolation of the flow velocities at cell faces to the location of the firebrand. In Eq. (6), $\hat{z}_r$ is the unit vector in the axial direction of the cylinder, and α is the incidence angle between the relative velocity vector and $\hat{z}_r$. Here, C_D is the drag coefficient which is determined by the following empirical correlation (Kelbaliyev, 2011; Oliveira et al., 2014)

$$C_D = \begin{cases} \frac{10}{\text{Re}_\alpha^{0.778}}, & \text{for } \text{Re}_\alpha \leq 0.1 \\ \frac{10}{\text{Re}_\alpha^{0.778}}\left[1 + \frac{\text{Re}_\alpha^{1.875}}{60 + 6.8\text{Re}_\alpha^{1.156}}\right], & \text{for } 0.1 < \text{Re}_\alpha \leq 6 \times 10^3 \\ 1.1, & \text{for } 6 \times 10^3 < \text{Re}_\alpha \leq 2 \times 10^5 \end{cases} \tag{7}$$

where $\text{Re}_\alpha = 2\rho a|\vec{V}_{\text{rel}}|\sin\alpha/\mu$ with μ representing air viscosity is the firebrand Reynolds number. In the non-stationary reference frame attached to the firebrand, the equation describing the rotational motion as given by the Euler rotation equations is:

$$\mathbf{I} \cdot \frac{d\vec{\omega}}{dt} + \vec{\omega} \times (\mathbf{I} \cdot \vec{\omega}) = \vec{T}, \tag{8}$$

where $\mathbf{I}$ is the moment of inertia tensor and $\vec{\omega}$ is the angular velocity of the firebrand. The torque $\vec{T}$ is given as

$$\vec{T} = \vec{T}_{\text{resis}} + \vec{T}_{\text{hydro}}, \tag{9}$$

where $\vec{T}_{\text{hydro}}$ is the torque due to hydrodynamic force, and $\vec{T}_{\text{resis}}$ is the frictional torque due to air resistance. The torque due to hydrodynamic force is caused when the center of pressure (location at which the net aerodynamic forces act) and the center of mass of the firebrand are non-coincident and is given by

$$\vec{T}_{\text{hydro}} = x_{\text{cp}} \mathbf{A} \cdot \left[\hat{z}_r \times (\vec{F}_D + \vec{F}_L) \right], \tag{10}$$

where, x_{cp} is the distance between the centre of pressure and the centre of mass of the firebrand (Marchildon et al., 1964). This location varies depending on the incidence angle of the firebrand and is computed via:

$$x_{\text{cp}} = 3b|\pi/2 - \alpha|/8\pi. \tag{11}$$

The sign of x_{cp} and hence the associated torque is determined by the sign of $\cos\alpha$ as given in Yin et al. (2011). In Eq. (10), **A** is a transformation matrix given as,

$$\mathbf{A} = \begin{pmatrix} 1 - 2(\epsilon_2{}^2 + \epsilon_3{}^2) & 2(\epsilon_1\epsilon_2 + \epsilon_3\eta) & 2(\epsilon_1\epsilon_3 - \epsilon_2\eta) \\ 2(\epsilon_2\epsilon_1 - \epsilon_3\eta) & 1 - 2(\epsilon_3{}^2 + \epsilon_1{}^2) & 2(\epsilon_2\epsilon_3 + \epsilon_2\eta) \\ 2(\epsilon_3\epsilon_1 + \epsilon_2\eta) & 2(\epsilon_3\epsilon_2 - \epsilon_1\eta) & 1 - 2(\epsilon_1{}^2 + \epsilon_2{}^2) \end{pmatrix}, \tag{12}$$

where ϵ_1, ϵ_2, ϵ_3 and η denote the quaternions (Goldstein, 2011).

Since the aerodynamic forces are calculated in the inertial reference frame, a transformation matrix is used to obtain the hydrodynamic torque in the particle reference frame. The components of the transformation matrix are calculated as a function of the four Euler parameters (also called quaternions).

In Eq. (9), the frictional torque is determined by:

$$\vec{T}_{\text{resis}} = -\rho |\vec{\omega}| ab^4 \left\{ 0.538 + 3.62 \left(\frac{\rho |\vec{\omega}| ab}{\mu} \right)^{-0.778} \right\} \vec{\omega}, \tag{13}$$

which acts a resistive torque with a tendency to reduce the angular velocity of the firebrand. The formulation in Eq. (13) was adapted from Oliveira et al. (2014) where a local rotational drag coefficient is integrated over the length of the cylinder to obtain the overall resistance. This torque is calculated in the firebrand rotational reference frame and hence a co-ordinate transformation is not required. In addition to the hydrodynamic/pitching and frictional torques, the local fluid strain/vorticity can also impact the rotation characteristics, thereby affecting the tumbling and spinning rate of firebrands (Voth and Soldati, 2017). In the current work, however, the impact of local fluid vorticity is not taken into account for two reasons. First, it is noted that heavier particles have longer response times and do not rapidly respond to fluid vorticity. Thus, they are not significantly spun up by the vorticity of the fluid, as discussed by Mortensen et al. (2007) for spherical particles. It is noted that Mortensen et al. (2007) found the response time for rotation to be 3/10 of the response time for translation. For this reason a spherical particle should respond faster to vorticity than to velocity alterations. However, these response times might be rather different for cylindrical particles and will depend on the orientation of the particle. Second, calculation of the interpolated fluid vorticity at particle positions would be computationally expensive. The orientation of the cylinder is tracked in terms of the Euler parameters instead of the Euler angles, thereby eliminating the singularity problem. Finally, the ordinary differential equations used to track the evolution of the Euler parameters (Yin et al., 2003; Njobuenwu and Fairweather, 2016) in terms of

the angular velocity are:

$$\begin{bmatrix} \dfrac{d\epsilon_1}{dt} \\ \dfrac{d\epsilon_2}{dt} \\ \dfrac{d\epsilon_3}{dt} \\ \dfrac{d\eta}{dt} \end{bmatrix} = \frac{1}{2} \begin{bmatrix} \eta\omega_x - \epsilon_3\omega_y + \epsilon_2\omega_z \\ \epsilon_3\omega_x + \eta\omega_y - \epsilon_1\omega_z \\ -\epsilon_2\omega_x + \epsilon_1\omega_y + \eta\omega_z \\ -\epsilon_1\omega_x - \epsilon_2\omega_y - \epsilon_3\omega_z \end{bmatrix}. \tag{14}$$

The time integration scheme for the fluid solver in WFDS is a second order Runge–Kutta type predictor-corrector method with a varying time step. The firebrand equations are solved with a time step twenty times smaller than that used for the fluid flow equations. A second order Adams Bashforth scheme (Press, 1992) is used for numerical integration of the firebrand equations.

3. Computational configuration

To generate the turbulent boundary layer, a computational domain with physical dimensions of $250 \times 40 \times 75$ m is used in the x, y and z directions, respectively. A grid resolution of $420 \times 67 \times 90$ is used with the grid stretched polynomially in the z direction. The first off-wall grid point is located such that it lies in the logarithmic region of the boundary layer ($y^+ \approx 1000$). The computational domain height used in this study corresponds to the atmospheric surface layer where the flow is insensitive to the earth's rotation (Kaimal and Finnigan, 1994). In the current study, a turbulent boundary layer with a free stream wind velocity of 18.8 m/s was considered. This velocity corresponds to the average measured wind speeds in the event of real-fire scenarios (case study of New Jersey fires). Also, the Beaufort scale characterizes this wind speed to be of scale 8, where wind speeds are defined as gales (strong winds) at which possibility of twigs breaking off from trees are high. Initially the Spalding law profile (Spalding, 1961) is imposed on the inlet with 10% turbulent intensity with a free stream velocity of 18.8 m/s and a boundary layer height of 25 m. As the flow develops, a realistic turbulent boundary layer was generated at the downstream location. Velocity components were then recycled from the recycle plane located at 80% of the length of the domain. At all times, the inlet boundary layer thickness was fixed to be 25 m. Once the turbulent boundary layer reached a statistically stationary state, firebrands were released continuously from a point at distinct heights of 20 m and 40 m, at locations within and above the boundary layer respectively. In total, 40,000 firebrands were tracked for each case and the maximum volume fraction of the firebrand with respect to the computational cell size was of the order of 10^{-5}. These release heights correspond roughly to the heights to which firebrands of the size considered in our work are lofted in wildfires.

The dimensions pertaining to the firebrand length and diameter were based on the experiments of Manzello et al. (2008) where real-scale fire experiments were performed by burning trees and the size distribution of firebrands collected from these experiments were reported. Most firebrands were cylindrical in shape with mean length and diameter of 40 mm and 3 mm respectively. These mean dimensions have been adapted for all firebrands in the current study. The firebrand length (40 mm) is an order of magnitude smaller than the grid size. Three firebrand densities of 70 kg/m³, 230 kg/m³ and 570 kg/m³ were investigated. These densities are representative of the wide range of firebrand densities observed in real fire scenarios. Here, 230 kg/m³ is the actual measured firebrand density (of material cedar wood) in the Oaklands hill fire conflagration (Pagni, 1993). The lower and higher limits of density correspond to density of charred firebrand and the density of unburned firebrand (cedar wood)
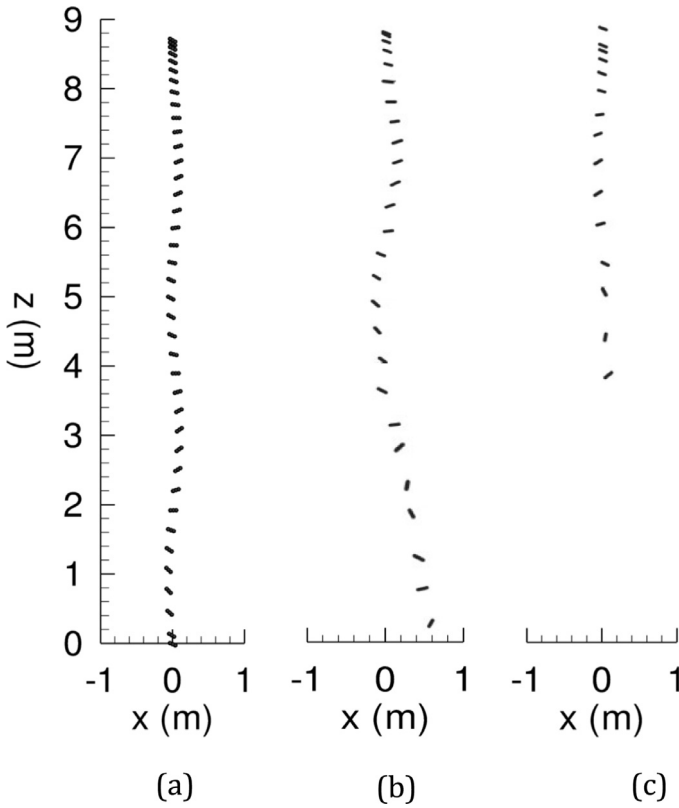
Fig. 3. Snapshots of a cylindrical firebrand falling in quiescent air; (a) simulation (current work); (b) simulation of Oliveira et al. (2014) and (c) experiment Oliveira et al. (2014).

Fig. 4. Instantaneous velocity magnitude on (a) the *xz* slice plane at the mid-section of domain (*y*=20 m) and (b) *zy* planes located at *x* = 62.5, 125.0, 187.5m.

(Reyes et al., 1992; Wilson and Brown, 1977) respectively. First, a test case was considered with the computational domain and Reynolds number equal to that studied in the work of Lund et al. (1998). After validating the recycling method with that of Lund et al. (1998), the same method was then applied to the turbulent boundary layer with free stream velocity of 18.8 m/s. For the case with the lowest density firebrand released from 40 m height, the domain in the *x* direction was extended to 400 m.

4. Results and discussion

First, a preliminary validation was performed for the presented dynamical model of the cylindrical firebrands against the experimental data of non-burning cylindrical firebrands released in quiescent air Oliveira et al. (2014). To simulate this experiment, firebrands with a density of 215.5 kg/m³ (balsa wood) of length and radius 80 mm and 5 mm, respectively, were considered. The major axis of the firebrand had an initial orientation of 60° with the vertical axis and it was released from a height of 8.7 m with zero initial velocity. The initial conditions and the properties of the firebrands are consistent with that used in Oliveira et al. (2014). The path followed by the firebrand during its descent in the current study and that obtained from both numerical and experimental works of Oliveira et al. (2014) are displayed in Fig. 3. In Fig. 3 (a), the firebrand position and orientation is shown at equal time intervals of 0.05 s from the time of release to the time of landing. The current results compare closely with both experimental as well as numerical results of Oliveira et al. (2014) up to a height of 5.5 m. It should be noted that the experimental data are unavailable after the cylindrical firebrand falls below ≈ 4 m. It took 2.08 s for simulated firebrands to land. This time was measured 1.8 s in the experiments and calculated 2.05 s in Oliveira et al. (2014). One reason
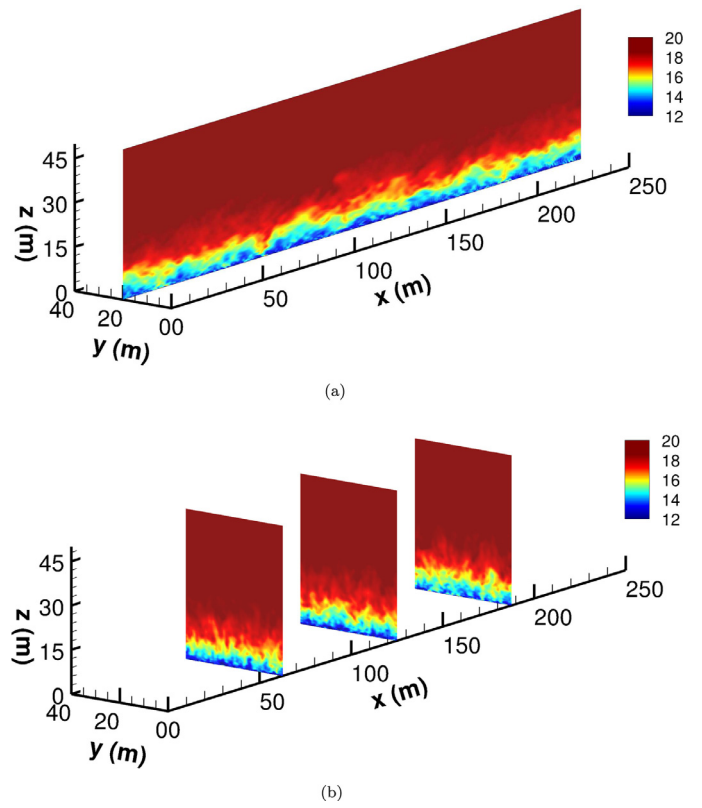
for the discrepancy between simulations and experiments at later times could be attributed to the simplified dynamical model that is implemented for the cylindrical firebrand. Also, uncertainties in measurements may contribute to the observed difference.

Now the results of the turbulent boundary layer study is discussed. In order to provide a pictorial overview of the flow field, contour plots of the instantaneous velocity magnitude within vertical planes in the computational domain are shown in Fig. 4. At the inlet, the boundary layer height is 25 m with a free-stream velocity of 18.8 m/s. Two release points considered for firebrands are located very close to the inlet at heights of 20 m and 40 m at the midplane in the spanwise direction. One point was within the boundary layer and the other above it.

Fig. 5 shows the mean flow velocity profile in the standard turbulent boundary layer coordinates, i.e., $u^+ = \bar{u}/u_\tau$ versus $z^+ = zu_\tau/\nu$, where $u_\tau = \sqrt{\tau_w/\rho}$ and τ_w is the wall shear stress. Displayed in this figure are two sets of data of the current study: one for $Re_\theta = 10^3$, which was for a case initially used to test the recycling method, as illustrated in the previous section, without firebrands; and the other for $Re_\theta = 10^6$, which used the same method in a larger domain where firebrands were simulated. The definition of Re_θ is give in sec 2.1. The mean streamwise velocity at a downstream location was calculated by averaging in both time and the homogeneous direction, after statistically stationary state is reached. Also, included in Fig. 5 are the computational data of Inoue and Pullin (2011), Spalart (1988), Rai and Moin (1993) and Lund et al. (1998) and experimental data of De Graaff and Eaton (2000). Good comparison is observed between the data obtained in the present work and the data available in literature for both the inner layer ($z^+ < 5$) as well as the log layer ($z^+ > 50$) of the turbulent boundary layer.

In Fig. 6 (a–d), the dimensionless Reynolds stresses are plotted against z/δ, where δ is the boundary layer thickness. Also, for com-
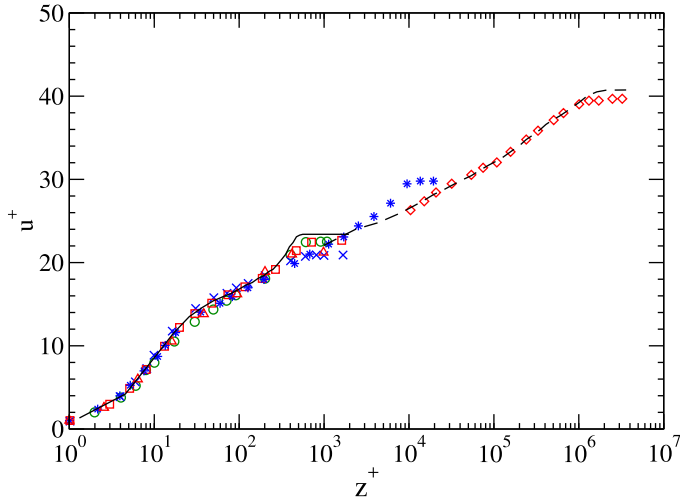
Fig. 5. Normalized mean streamwise velocity of the flow plotted against the wall normal coordinate. Solid and dashed lines indicate the test cases with $Re_\theta = 10^3$ and 10^6, respectively. Symbols are the computational data of Inoue and Pullin (2011) $\diamond$, Wu and Moin (2009) $\triangle$, Lund et al. (1998) $\square$, Rai and Moin (1993) $\times$, Spalart (1988) $\circ$; and experimental data of De Graaff and Eaton (2000) $\ast$.

parison, the data available in literature (symbols) are plotted using the same notation as in Fig. 5. The Reynolds stresses are normalized by the friction velocity in this figure. For the simulated case of $Re_\theta = 10^3$, the boundary layer was resolved up to $z^+ = 1$, which is the region close to the wall. A good agreement between this case and the data available in the literature is seen in this region. On the other hand, for the simulated case of $Re_\theta = 10^6$, which uses a significantly coarser grid as the Werner-Wengle wall model was applied, the first off-wall cell lies in the logarithmic region of the boundary layer. The sharp rise observed in panels (a–c) for this case in the inner region very close to the wall, which is in disagreement with other cases, is because the wall model provides only an estimate of the velocity components in this region. However, comparison away from the wall is very good.

In the rest of this section, statistics pertaining to the firebrand positions and velocities are presented and discussed for three firebrand densities and two release heights. A statistical approach is essential in characterizing the behavior of firebrands carried in turbulent flows, as the trajectories of individual firebrands are distinct although released under identical initial conditions. This distinction is attributed to the uniqueness of the sequence of the flow velocities that each firebrand samples from release to landing in
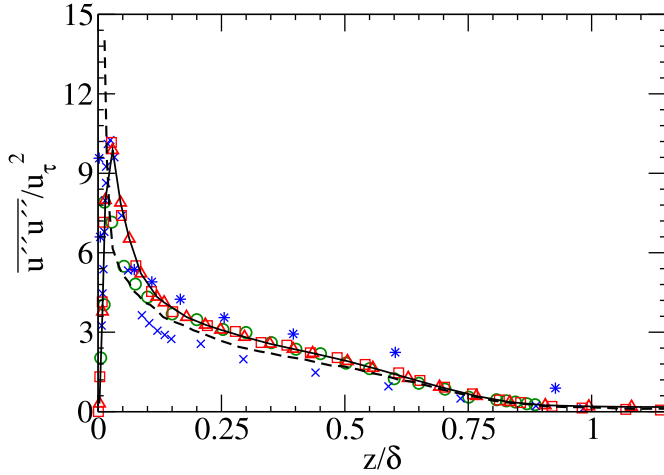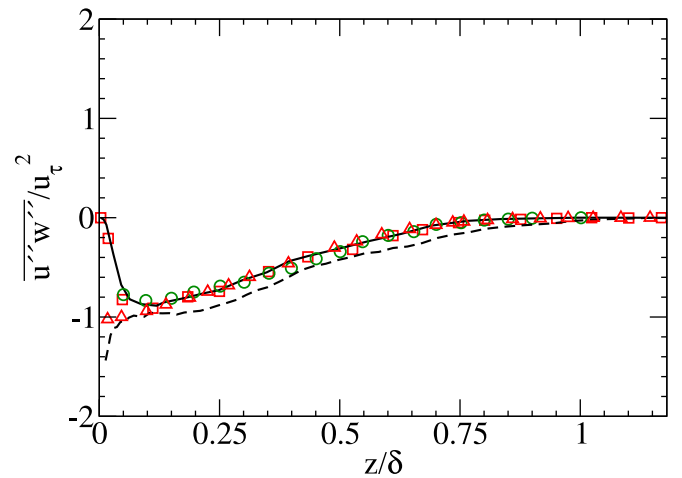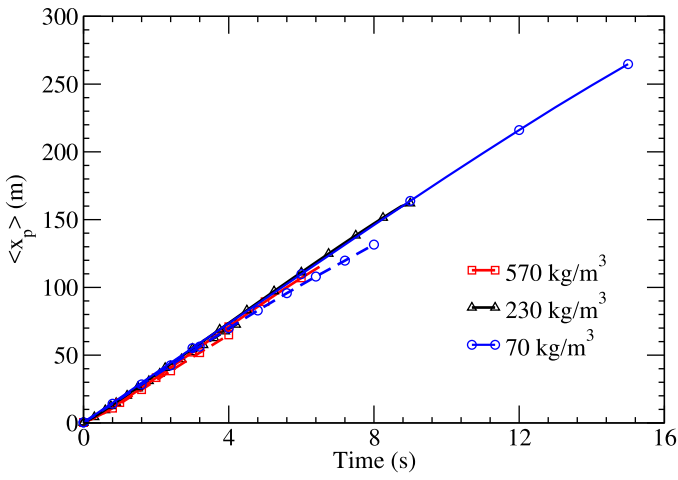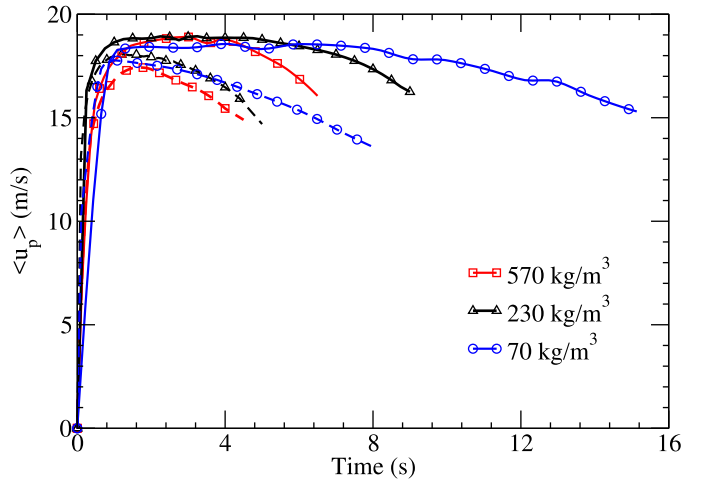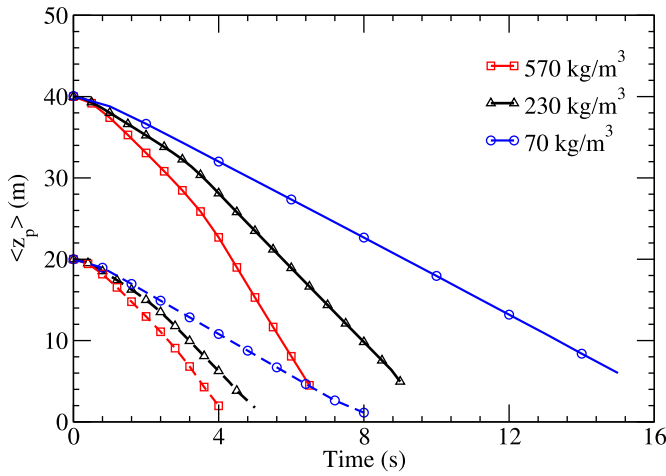

(a)
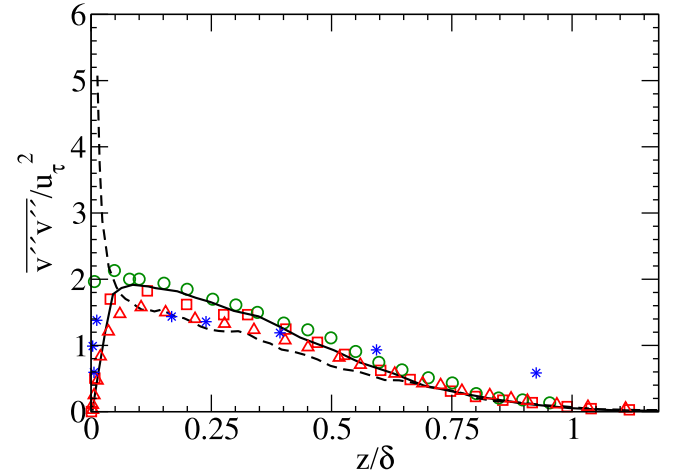
(b)
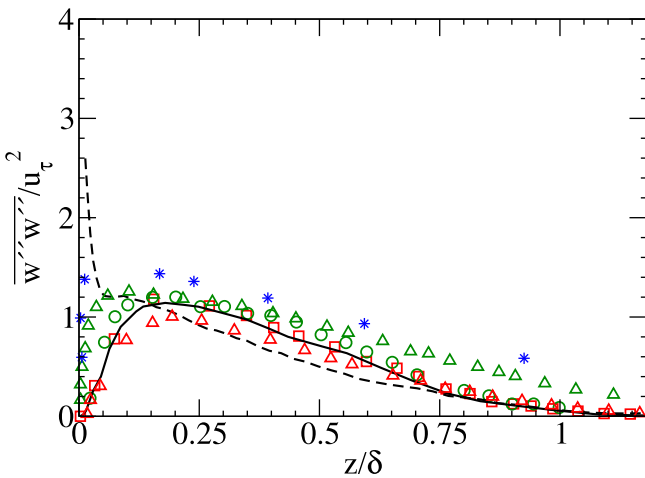
(c)

(d)

Fig. 6. Reynolds stresses normalized by the shear velocity versus the wall coordinate normalized by boundary layer thickness. See the caption of Fig. 5 for the legend.
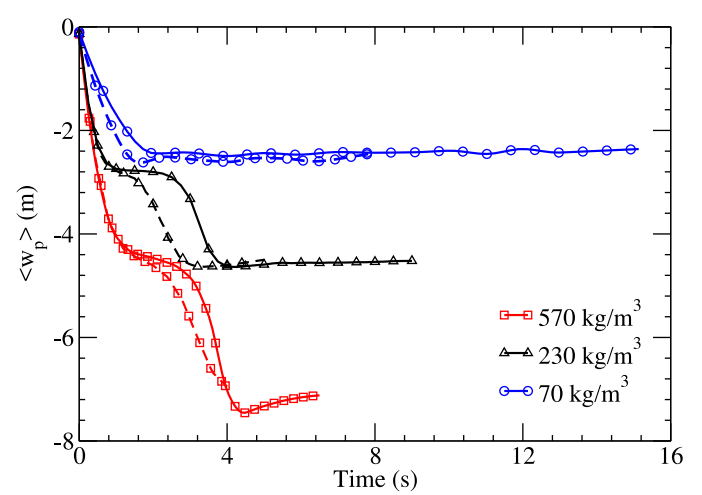
Fig. 7. Temporal variation of the mean (a) streamwise and (b) vertical components of firebrand positions for release heights of 20 m (dashed lines) and 40 m (solid lines).
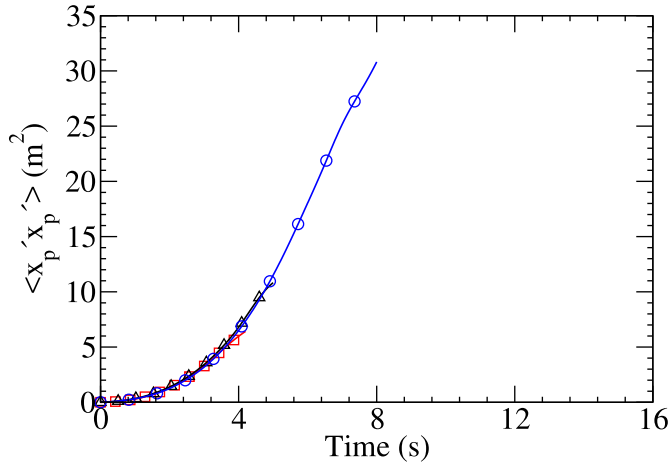

Fig. 8. Temporal evolution of the mean (a) streamwise and (b) vertical components of the firebrands velocities for release heights of 20 m (dashed lines) and 40 m (solid lines).

turbulence, and is manifested by the uniqueness of the landing location of the firebrand, as evident from the results to be presented. The statistical quantity associated with each curve in the following figures are calculated using an ensemble of flying (suspended) firebrands released from the same point. On the other hand, the time that each firebrand takes to land is different. The curve is displayed until the time right before the first firebrand in the ensemble lands.

In Fig. 7, the time evolution of the streamwise and vertical components of the mean firebrand position, $\langle x_p \rangle$ and $\langle z_p \rangle$, respectively, is displayed for all simulated cases. Here, $\langle \ \rangle$ indicates ensemble averaging over firebrands. As seen in Fig. 7(a), $\langle x_p \rangle$ exhibits an almost linear functionality with time. The streamwise firebrand position is largely determined by the streamwise component of carrying flow velocity. Since the mean of this component does not vary significantly in the streamwise direction, the streamwise firebrand position varies almost linearly. On the other hand, in the vertical direction, the terminal velocities attained by firebrands are largely a function of firebrand densities. Thereby, the effect of density on the mean position and dispersion is largely seen on the vertical di-

rection. The firebrands with the lowest density of 70 kg/m^3 which were released from a height of 40 m travelled the longest distance (~ 275 m) while the ones with the highest density which were released from a lower height of 20 m, travelled the shortest distance (~ 75 m). For firebrands with identical densities, the ones released from the height of 40 m, take approximately twice the time to reach the ground as compared with the ones released from the height of 20 m. As evident in Fig. 7(b), the gravitational force acting on larger density firebrands is more dominant so they descend faster than lower density firebrands. Also, the mean elevation of firebrands almost linearly decreased with time for the lowest density firebrands.

The time variation of the streamwise and vertical components of the mean firebrand velocity is shown in Fig. 8. Here, u_p, v_p and w_p are the firebrand velocity components in x, y and z directions respectively. The mean firebrand velocity in the spanwise direction is cacluated to be negligible so it is not displayed in this figure. As can be seen in Fig. 8(a), the mean streamwise velocities of firebrands increase very rapidly to values close to the local flow velocity, which is in the range 17–18.8 m/s depending on their re-
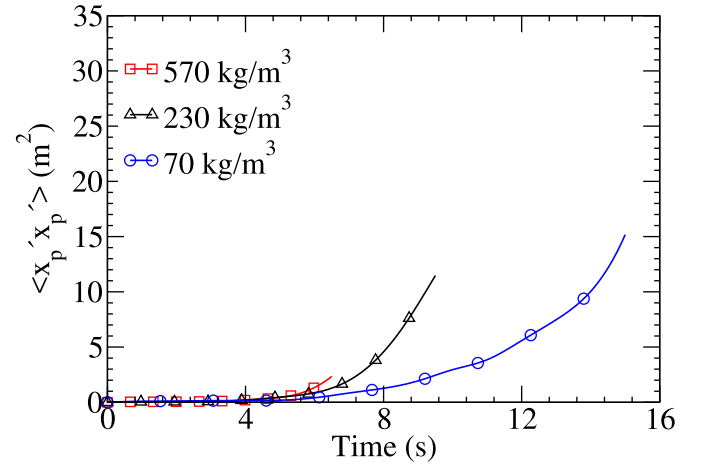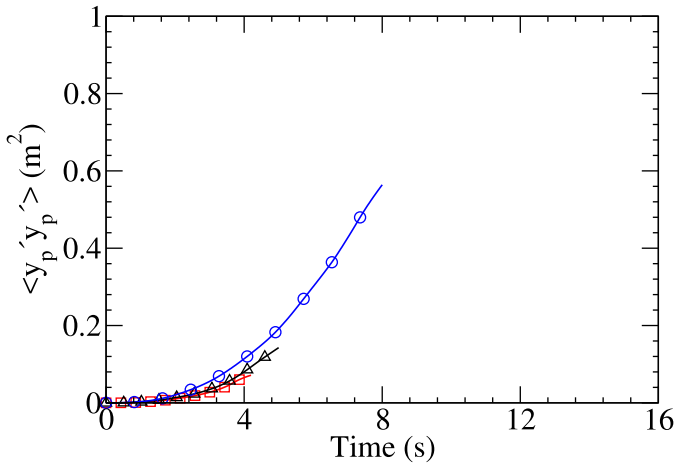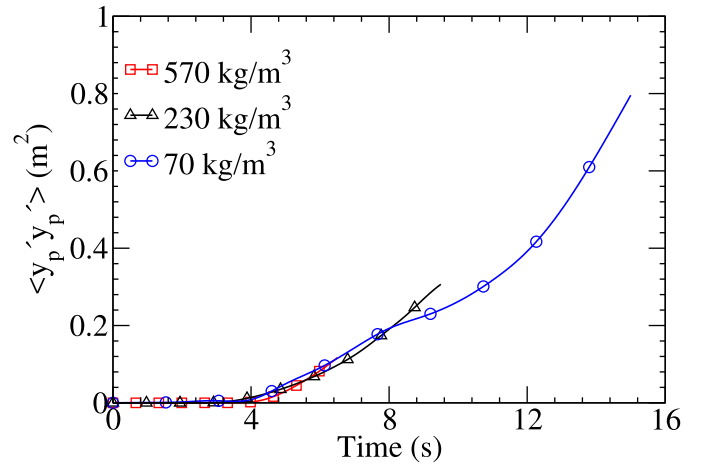
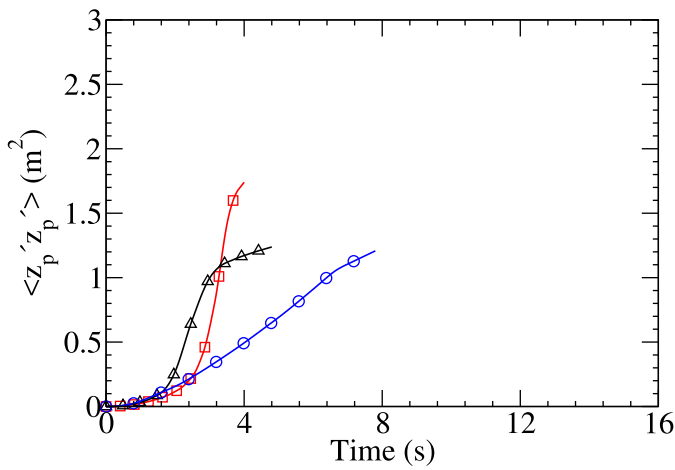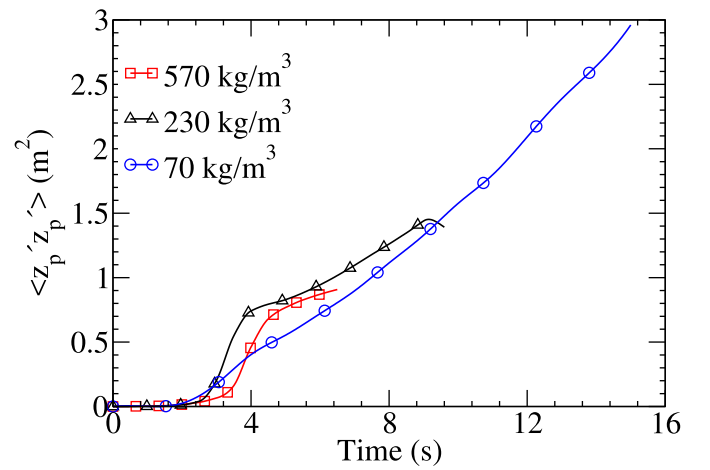**Fig. 9.** Temporal evolution of turbulent dispersion of firebrand in the streamwise (top row), spanwise (midde row) and vertical direction (bottom row) for firebrands released from a height of 20 m (left panels) and 40 m (right panels).
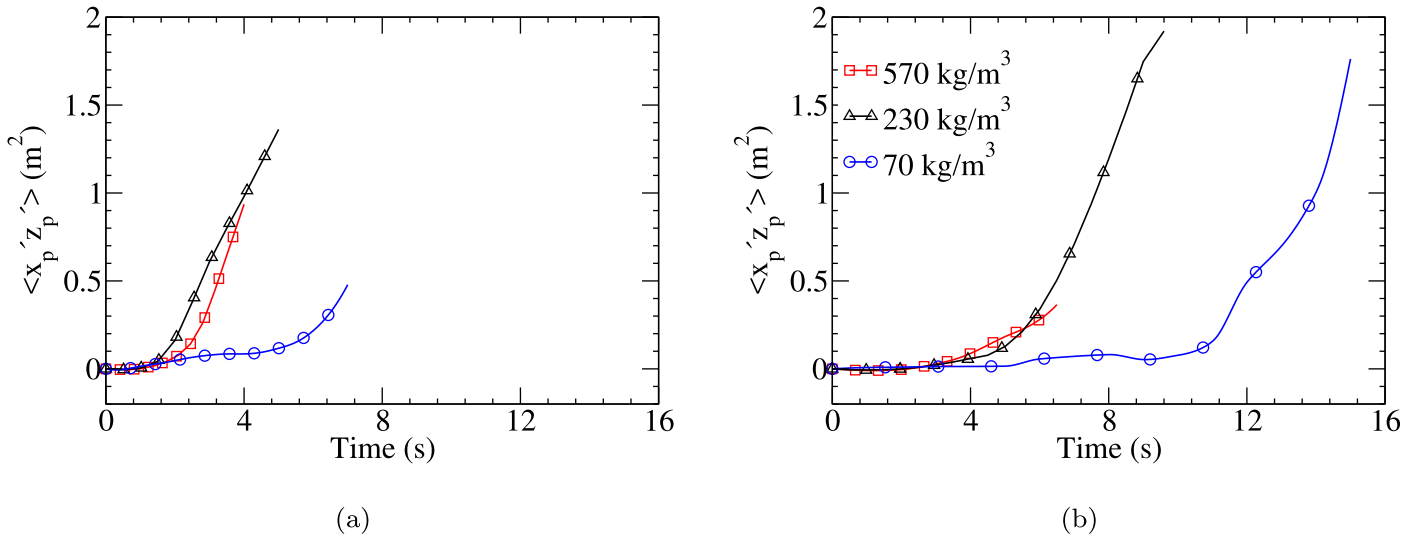
Fig. 10. Temporal evolution of variation of the off-diagonal turbulent dispersion components. Firebrands released from 20 m and 40 m height are shown on the left and right panels respectively.

lease heights. This increase is because of an initial large magnitude of the drag and lift forces, as the relative velocities between the firebrands and their local flows are initially large (see Eq. (5) and (6)). The gravitational forces in the vertical direction are dominant, as evident by the negativity of $\langle w_p \rangle$ in Fig. 8(b), resulting in the descent of the firebrands. In a boundary layer, since the mean streamwise flow velocities decrease with a reduction in elevation, in the average sense, the drag forces in the streamwise direction decrease while firebrands descend. This is the reason for the decrease of $\langle u_p \rangle$ after the initial times, as seen in Fig. 8(a). It is seen in Fig. 8(b) that $\langle w_p \rangle$ becomes almost constant prior to the firebrands reaching the ground. This constant value can be regarded as the mean terminal velocity. At the terminal velocity, the forces due to drag and lift are balanced by the force of gravity in the vertical direction so the acceleration of the firebrand is zero. Initially the firebrands have no oscillations upon release. As they begin to descend, the firebrands begin to oscillate about the 90° angle, which is also a stable equilibrium point for falling cylindrical rigid bodies (Yin et al., 2003; Oliveira et al., 2014). Once the aerodynamic forces balance the gravitational force, the firebrands attain the terminal velocity and the oscillations are damped out as they fall stably at the 90° angle. Firebrands with lower densities have shorter time response and hence the oscillations damp out quickly. On the other hand, firebrands with higher densities with longer response times oscillate for a longer period of time and hence the first plateau is observed. However, at later times when the forces balance each other, $\langle w_p \rangle$ asymptotes towards the terminal velocity.

It is observed that firebrands with same densities released from different heights reach the same mean terminal velocity. The firebrands with the least density of 70 kg/m³ reach a mean terminal velocity of 2.5 m/s in a time period of 2 s, while firebrands with the highest density of 570 kg/m³ reach a mean terminal velocity close to 7.8 m/s in a time period of 4 s. Based on the wind tunnel experiments, Tarifa et al. (1965) proposed the terminal velocity assumption wherein firebrands were assumed to travel at their terminal velocity at all times. This assumption has also been widely used to track the motion of firebrands (Albini, 1979; Himoto and Tanaka, 2005). However, the terminal velocity approximation may be applicable for simplified wind and plume models (Koo et al., 2012) and is not suitable for turbulent flows. Such flows have an effect of modulating the velocity of the firebrand, thereby inhibiting the firebrands from achieving the terminal velocity at all times.

As evident in the Fig. 8(b), it must be emphasized that depending on the density and the background wind, a time delay exists in achieving the terminal velocity. Thus the terminal velocity approximation would incorrectly predict the position of firebrands and will not hold for the scenarios described in this paper.

To help in understanding the extent of spatial dispersion of firebrands in various directions, the dispersion tensor defined by $\langle x'_{p,i}(t) x'_{p,j}(t) \rangle$, where $x'_{p,j}(t) = x_{p,j}(t) - \langle x_{p,j}(t) \rangle$, is calcuated. The temporal evolution of firebrand dispersion is displayed in Figs. 9 and 10. For all the cases, it is seen that the dispersion is zero at the release time and increases over time. This zero initial value is attributed to the release of firebrands from a fixed point in every simulation. For the cases with release height of 40 m, since the release point is in the outer layer and the flow is laminar in this layer, firebrands descend initially without experiencing turbulence. Hence, dispersion for the first few seconds do not gain an appreciable value until firebrands enter the boundary layer which is turbulent.

On the other hand, the initial time for dispersion to gain an appreciable value is shorter in the cases where the release point is at 20 m above the ground, which is in the turbulent boundary layer. For both release height cases, it is seen that the dispersion of firebrands is higher for lower firebrand density since it has less inertia. Dispersion in the streamwise direction is found to be larger than the other components. This is because, as evident from Fig. 6, the magnitude of the Reynolds stress for the carrying phase is the largest in the streamwise direction. Hence, the turbulent fluctuations in the background flow has an effect of dispersing the firebrands more significantly in this direction. Also, from Fig. 6, the magnitude of Reynolds stresses in the spanwise direction is greater than the vertical component. However for the firebrands, as shown in Fig. 9 it is observed that the vertical component of dispersion is greater than the spanwise component. This behavior is observed because, in the vertical direction, since the densities of the firebrands are much larger than the density of the carrier flow, the gravitational force acting on the firebrand is dominant in comparison to the forces acting on the firebrand in the spanwise direction. For the same reason, the lighter firebrands for both the release height cases disperse laterally more than the heavier firebrands. Hence, the overall effect of the turbulent boundary layer on the firebrands is to cause significant dispersion in the streamwise direction. In Fig. 10 the variation of the most significant off-
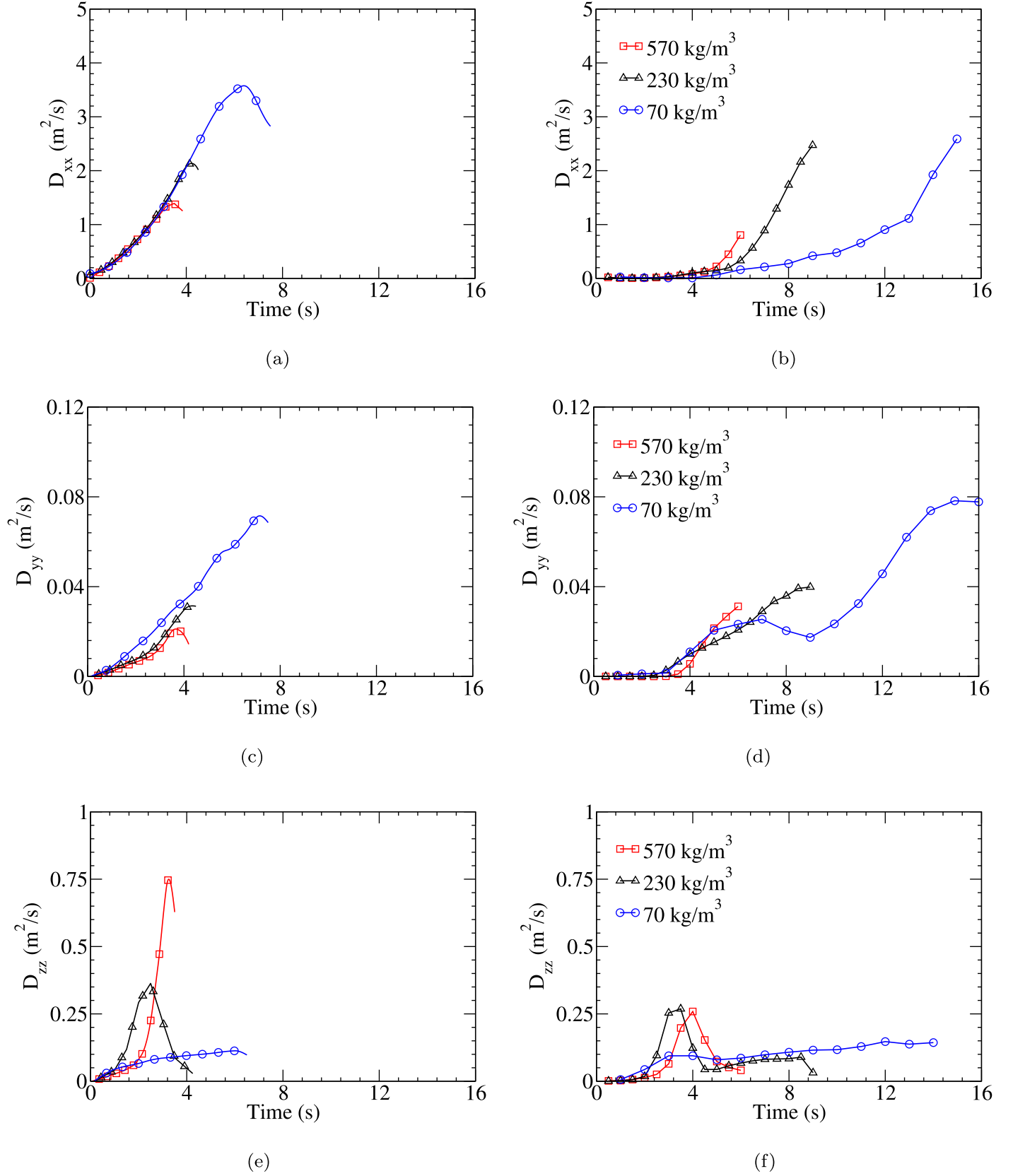
Fig. 11. Temporal evolution of turbulent diffusivity components of firebrands in streamwise (top row), spanwise (middle row) and vertical (bottom row) directions for the release height of 20 m (left panels) and 40 m (right panels).
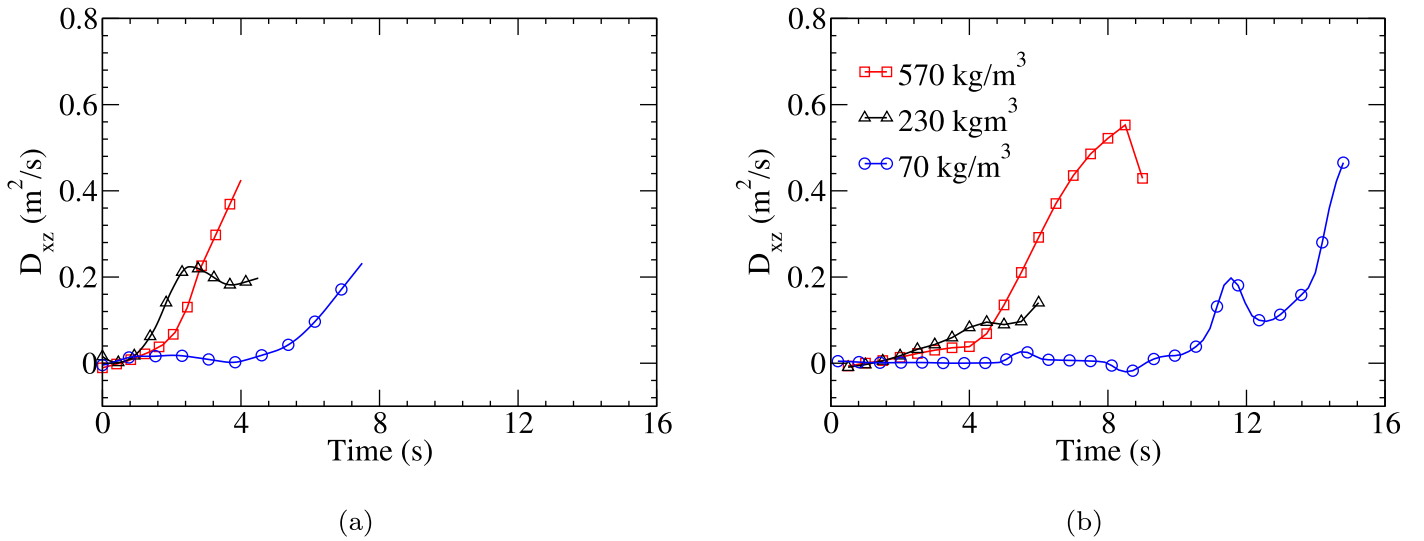
Fig. 12. Time evolution of the off-diagonal components of the turbulent diffusivity for a release height of 20 m (left panels) and 40 m (right panels).

diagonal dispersion component is shown. Fig. 10 does not include a panel for $\langle x'_p y'_p \rangle$ and $\langle y'_p z'_p \rangle$ as these dispersion components remain very close to zero at all times in the simulations. The negligible value of the off-diagonal dispersion components of the firebrands is attributed to the less dominant shear stresses of the carrier flow field calculated as a function of the spanwise direction. However, the quantity, $\langle x'_p z'_p \rangle$ is significant owing to the larger fluctuations in the streamwise and vertical components of velocity.

The rate at which firebrands are spatially deposited is crucial to understanding the phenomena of rate of fire spread which in turn is a function of firebrand release height, density and ambient wind speed. In Figs. 11 and 12, the turbulent diffusivity of firebrands (Taylor, 1922; Crowe et al., 2011; Böning, 1988) defined by

$$D_{ij}(t) = \frac{1}{2} \frac{d\langle x'_{p,i}(t) x'_{p,j}(t) \rangle}{dt}, \quad (15)$$

is plotted against time. The diffusivity tensor, indicates the rate at which firebrands are spatially dispersed. In the work of Taylor (1922), it was demonstrated that, when gravitational effects on particles are neglected, the diffusivity of particles correlates with that of the carrier flow. It was also emphasized in several works (Csanady, 1963; Snyder and Lumley, 1971; Rogers and Eaton, 1991; Kaftori et al., 1995; Armenio and Fiorotto, 2001) that the turbulent fluctuations in the carrier flow can significantly impact the diffusion of particles with low inertia. In the current study however, the density of firebrands is much greater than the density of the air/carrier flow. Since the high inertia firebrands rapidly descend and encounter different fluid regions, their diffusion is not well correlated with that of the carrier flow. It is found that the diffusivity of the firebrands in the streamwise and the spanwise directions increases with time for all the cases. This is due to the increased turbulent fluctuations encountered within the turbulent boundary layer. For a given release height, the firebrands with the least density have larger variances and hence are more diffusive. In both spanwise and streamwise directions, the diffusivity of firebrands having the least density is almost twice as that of the firebrands with the highest density at times close to deposition on the ground. However, in the vertical direction, the diffusivity of firebrands peaks and then plateaus at the time of deposition. This behavior is observed because the firebrands descend through the turbulent boundary layer where turbulent fluctuations affect its motion and increase its diffusivity. With further increase in time, the gravitational force acting on the firebrand

balances the aerodynamic forces and the acceleration of the firebrands tend to zero, hence decreasing its diffusivity. This decrease in diffusivity at terminal/asymptotic velocities is also discussed by Csanady (1963) in the context of turbulent diffusion of heavy particles. The off-diagonal component shown in Fig. 12 is representative of the rate of change of correlations of the fluctuation in displacements. Here, similar to dispersion, among all off-diagonal diffusivity components D_{xz} had a significant value. Since the fluctuations in spanwise displacements is small, the other components D_{xy} and D_{yz} remained close to zero. Overall, in Figs. 9–12, the statistical quantities relating to firebrands such as turbulent dispersion and diffusivity are presented. From these statistics, the impact of the flow turbulence for varying firebrand densities is understood. While the dispersion tensor helps to understand the extent to which firebrands are dispersed in various directions, the turbulent diffusivity tensor provides further information regarding the rate at which firebrands are spatially dispersed. It is seen that these quantities are largely a function of the firebrand release height and density.

Firebrand velocity variances are shown in Fig. 13. It is seen that they are zero at the beginning, which is attributed to the release of firebrands with zero velocities. After the release, the variances increase for the 20 m height cases whereas they remain very close to zero for the first few seconds and then increase for the 40 m ones. The reason for this difference is illustrated here. The 20 m height release point is located within the turbulent boundary layer whereas the 40 m one is above it. The flow above the boundary layer is laminar, as evident by vanishing Reynolds stresses for large z^+'s in Fig. 6. Thus, the firebrands released from the 40 m height point do not encounter turbulence until they enter the boundary layer. As a result, they possess identical velocities at identical times during their flight from the release point to where they enter the boundary layer. Hence, the firebrand velocity variances are zero and their trajectories are identical while outside of the boundary layer. As could be seen in Fig. 13, the variance of the firebrand velocity in the spanwise direction is the least among all directions for a given density and release height. A unique noticeable aspect is with panels (e) and (f) in Fig. 13. That is a sharp peak in the variance of the velocity in the vertical direction for two largest densities. This peak is a result of the competition between the hydrodynamic force, viz., the combined drag and lift forces, and the body force, viz. the combined gravitational and buoyancy forces. While the former is under the influence of turbulence, the latter
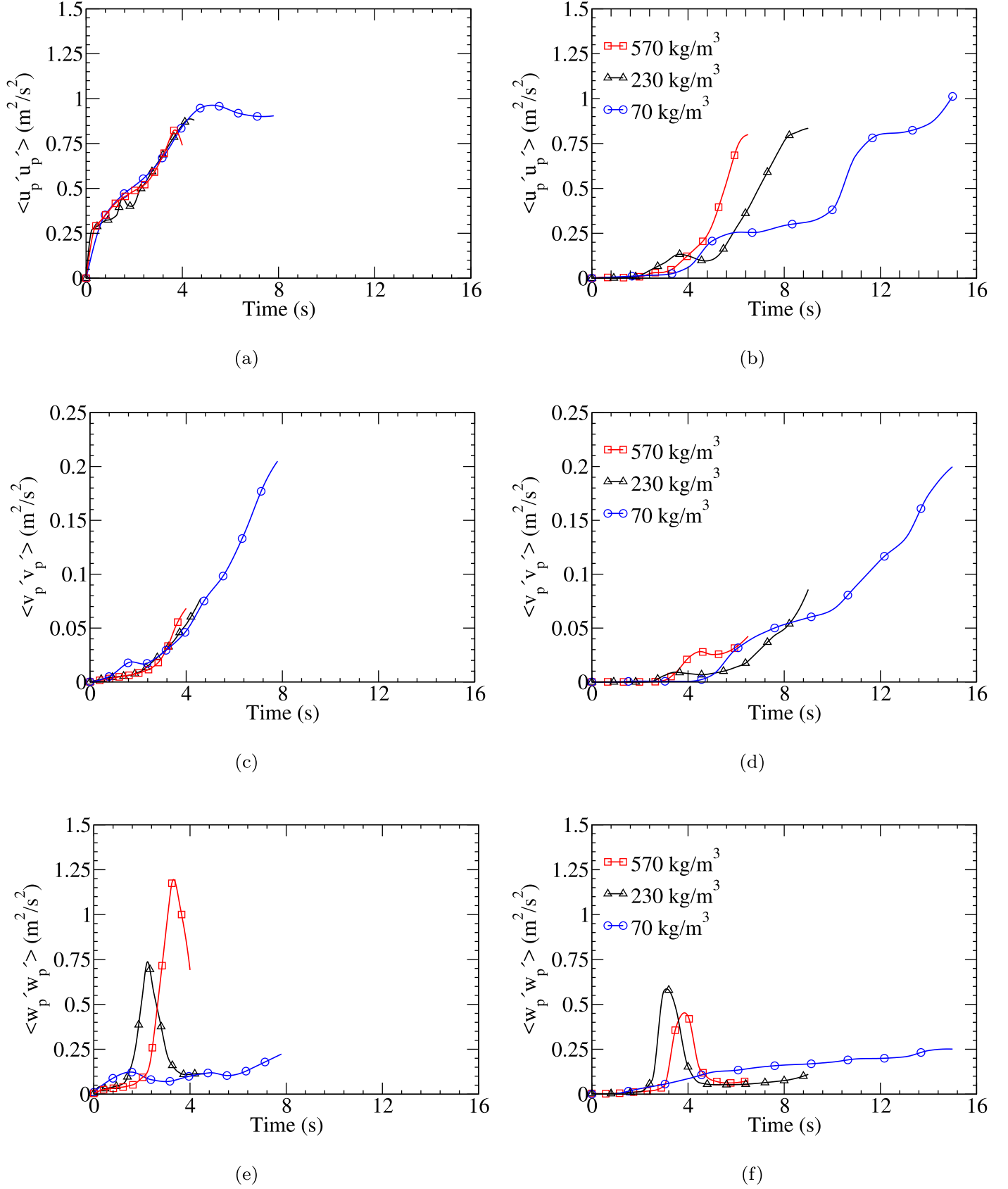
Fig. 13. Temporal evolution of the variances of the firebrand velocities for the release heights of 20 m (left panels) and 40 m (right panels).
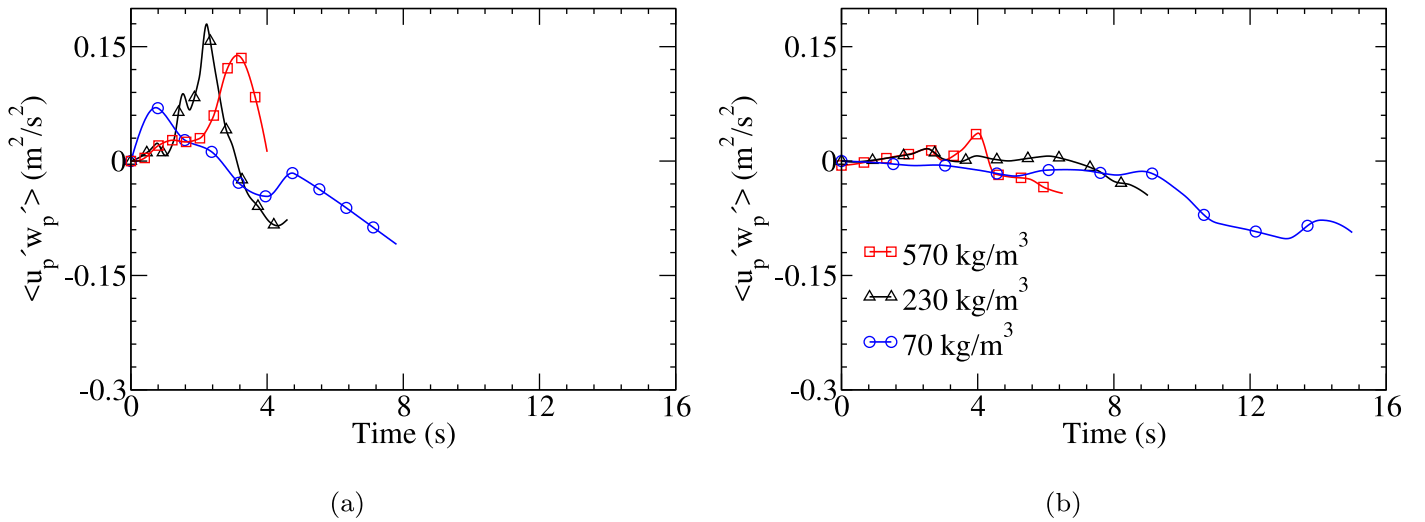
Fig. 14. Time evolution of the co-variances of firebrand velocities for the release heights of 20 m (left panels) and 40 m (right panels).

is not. Starting with zero values, vertical velocity variances grow because of the turbulence in the flow. On the other hand, as time progresses, firebrands gain a mean terminal velocity as the projection of the hydrodynamic force in the vertical direction balances with the body force in the average sense. The vertical velocities of heavier firebrands deviate slightly from the mean terminal velocity (see Fig. 8(b)).

Fig. 14 displays the covariance of the firebrand velocities $\langle u'_p w'_p \rangle$ vs time. The other co-variances are not shown, as they do not have appreciable values. For the firebrands released at the 20 m height, the covariance $\langle u'_p w'_p \rangle$, increases upto the time at which the terminal velocity is attained. However, at later times, $\langle u'_p w'_p \rangle$ tends to a negative value and varies similar to the shear stress of the carrier flow, which is displayed in Fig. 6. In case of the firebrands being released outside the boundary layer, the initial peak in $\langle u'_p w'_p \rangle$ is less pronounced as the firebrands reach their terminal velocity just before entering the turbulent region. Hence, at early times the covariance is close to zero as the firebrands descend through the free-stream region and later becomes negative due to the shear stress of the carrying flow.

The likelihood of ignition by spotting will be higher if a large number of deposited firebrands are accumulated in close proximity of each other. Thus, characterization of the pattern of deposition of firebrand will help to delineate areas prone to spotting ignition. The number density of the deposited firebrands, defined as the number of firebrands deposited per unit area, is a variable that can be calculated to quantify the particle accumulation. On the other hand, it can be shown that the number density is proportional to the probability distribution function (PDF) of the streamwise and spanwise coordinates of the deposited firebrands. In Fig. 15, the contour plots of this function are displayed (x and y axes do not use the same scale). If f indicate this PDF, it is calculated by:

$$f(x, y) = \frac{1}{nh^2} \sum_{p=1}^{n} K\left(\frac{x - x_p}{h}, \frac{y - y_p}{h}\right) \qquad (16)$$

where, h is the bandwidth parameter, n is the total number of the deposited firebrands and $K(x, y)$ is called the smoothing kernel, which is calculated by $K(x, y) = K(x) \cdot K(y)$ in the current work, where $K(x)$ is a standard normal distribution. Also, x_p and y_p are the coordinates of a deposited firebrand in the streamwise and spanwise directions, respectively. It is noted with the given definition, $f(x, y)$ satisfies the normalization condition, meaning that its integration over the area is unity. Here, f also indicates the proba-

bility density function of the landing coordinates of a released firebrand.

In Fig. 15, the contour lines of the PDF of the deposited firebrands are displayed. In each panel of Fig. 15, the innermost contour line indicates the region with the highest probability of deposition. The contour lines resemble ellipses with minor and major axes in the spanwise and streamwise directions, respectively. This appearance is an indication of a larger dispersion in the streamwise direction than in the spanwise direction. The streamwise distribution of the firebrands with the lowest density 70 kg/m³ and the release height of 40 m is almost 1.6 times greater than the release height at 20 m. This factor is found to decrease to 1.2 when the firebrand density is increased to 230 kg/m³ and stays nearly equal to 1.0 for the case with firebrand density of 570 kg/m³.

Normalized statistics pertaining to the landing locations of the firebrands for all cases is reported in Table 1. Here, statistical quantities are normalized by the release height z_r. They help to characterize the PDF's displayed in Fig. 15. Table 1 confirms the mean streamwise coordinate of the deposited firebrands $\langle x_p \rangle$ increases as the firebrand density decreases. A similar trend is seen for the variances in the streamwise and spanwise directions. Except for the case with firebrand density of 570 kg/m³, firebrands released from the 40 m height have a smaller normalized streamwise variance, as compared to that from the 20 m release height. This difference is because the firebrands falling from the 40 m elevation attain a terminal velocity just before reaching the turbulent boundary layer and also owing to inertia, these firebrands are less susceptible to be influenced by the turbulent fluctuations as compared to the case with release height of 20 m. For the lowest density firebrand, when released from a height of 40 m, the ratio of the streamwise and spanwise variances is the largest ~ 45. The distribution of the deposited firebrands appears symmetric in the spanwise direction, as seen in Fig. 15, because of a statistical symmetry of the carrier flow in this direction and that all firebrands are released at the symmetry plane located at $y = 20$ m. Our calculations also showed that $\langle y_p \rangle = 20$ m for the deposited firebrands in all cases.

Also, shown in Table 1 are the multivariate skewness and kurtosis of the PDF to quantify the deviation of the PDF from a bivariate Gaussian distribution. For a Gaussian distribution, the multivariate skewness is zero. From Table 1 it is seen that the skewness is nonzero and positive in all cases. For the cases where firebrands were released from a height of 40 m, the deposition of firebrands is more skewed. Here, firebrands traverse through the turbulent boundary layer for a longer period in time as compared to
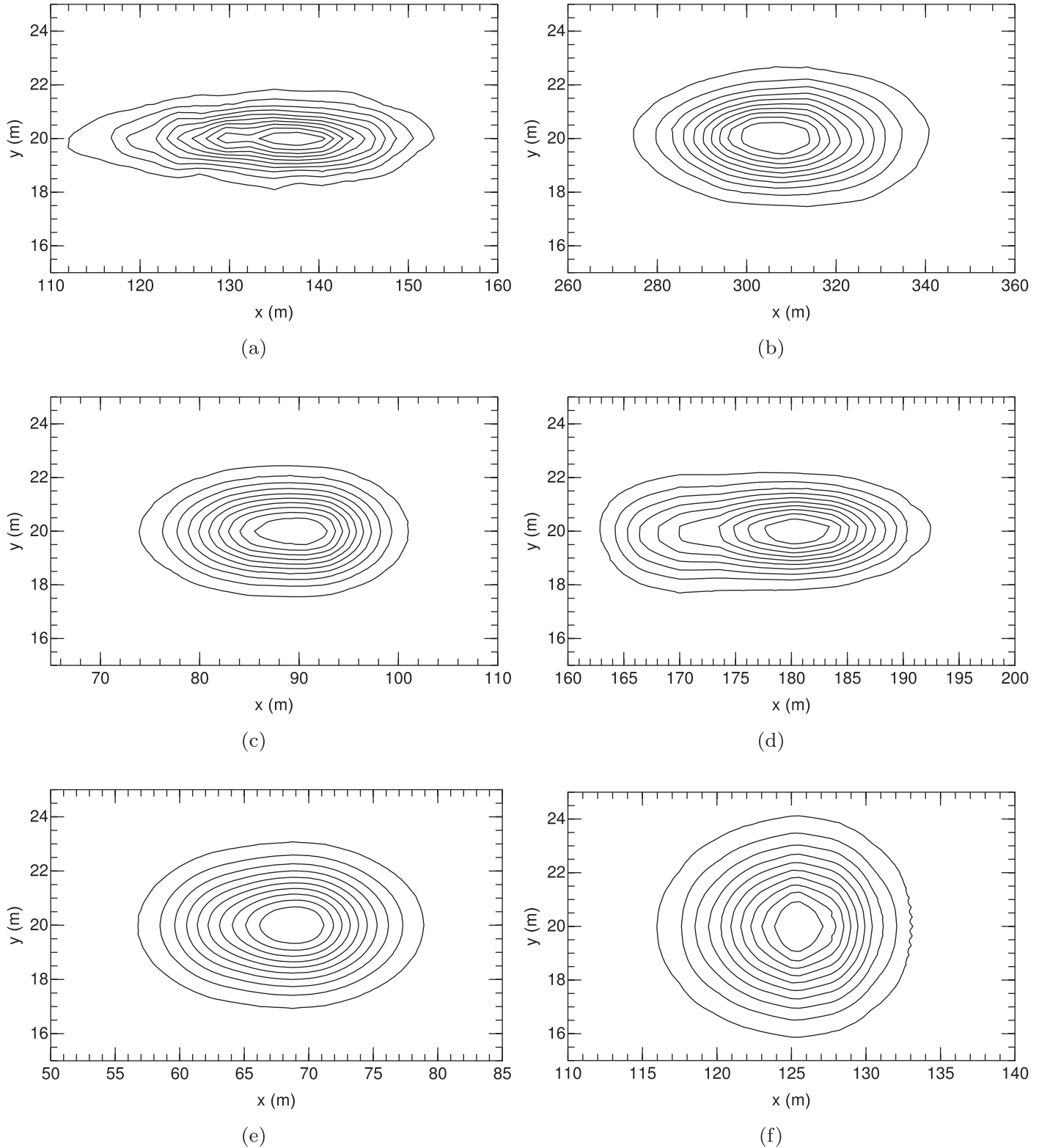
(a)

(b)

(c)

(d)

(e)

(f)

Fig. 15. Contour plots of the probability distribution of deposited firebrands for the release height = 20 m (left column) and 40 m (right column) for $\rho_p = 70$ kg/m^3 (top row), 230 kg/m^3 (middle row) and 570 kg/m^3 (bottom row). The innermost contourlines have a value of 0.02. The contourline values decrease with an increment of 0.002 from the innermost to outermost contours.

the ones released from a lower elevation. However, for the lowest density case (70 kg/m^3) released from a height of 40 m, the ground distribution is less skewed. Here, the firebrands first travel through the free-stream velocity region, where turbulence is lacking in the carrier flow, and then through the turbulent boundary layer where

fluctuations in flow velocities become significant. When the density of the firebrand is low, the firebrands reach their terminal velocity well before entering the turbulent boundary layer. Once the firebrand reaches its terminal velocity, which is the maximum velocity attained in the vertical direction, it is not largely affected by

Table 1
Normalized statistics pertaining to the distribution of deposited firebrands.

Release height (m)	Density (kg/m^3)	$\langle x_p \rangle / z_r$	$\langle x_p' x_p' \rangle / z_r^2$	$\langle y_p' y_p' \rangle / z_r^2$	$\langle x_p' y_p' \rangle / z_r^2$	Bivariate skewness	Bivariate kurtosis
20	570	3.40	0.07	0.01	1.00E−4	0.04	8.21
	230	4.40	0.10	0.01	7.50E−5	0.03	8.36
	70	6.71	0.22	0.01	−2.00E−4	0.08	8.59
40	570	3.12	0.01	2.73E−3	6.25E−5	0.12	8.78
	230	4.44	0.03	2.83E−3	2.18E−4	0.28	9.11
	70	7.70	0.15	3.43E−3	2.94E−5	0.08	8.64

the fluctuations in the turbulent boundary layer. Hence, the deposition is less skewed as compared to the other cases. Also shown in Table 1 is the kurtosis for various cases. Based on Mardia's kurtosis test (Mardia, 1970; 1974), for a bivariate distribution, the kurtosis for a normal distribution is eight. For the bivariate PDF shown here, for all the cases, the kurtosis is greater than eight and hence we conclude that the distribution is leptokurtic. Except for the cases with firebrand densities 570 and 230 kg/m^3 released at 20 m height, the calculated multivariate kurtosis deviated more than 5% of that of a normal distribution.

5. Conclusions and summary

In the current work, the impact of turbulence in the ambient wind on the transport and deposition of firebrands in a turbulent boundary layer was studied. Specifically, the motion of firebrands was tracked for the spotting range classified to be intermediate wherein firebrands are carried mainly by the turbulent ambient wind, and the flow field is essentially uninfluenced by heat release. In a real fire scenario, firebrands are generated in various shapes and sizes, and mass and size distributions. This study is limited to cylindrical firebrands with the choice of the physical properties of firebrands motivated by the tree burn experiments of Manzello et al. (2007, 2009) where generated firebrands were predominantly cylindrical in shape. A Lagrangian particle tracking module was developed to solve for the coupled translational and rotational motion of cylindrical firebrands. This model was then integrated with the Wildland-urban Fire Dynamics Simulator (WFDS) to solve for the background air flow turbulence. Using the rescaling and recycling method of Lund et al. (1998), a turbulent boundary layer was generated. The statistics of the resulting flow field obtained from such a boundary layer was then validated against data available in the literature. Firebrands were released consecutively in the turbulent boundary layer at points within and above the boundary layer edge with identical physical properties and initial velocities. The path followed by the firebrands and ground deposition was studied for three cases of densities ranging from 570 to 70 kg/m^3. Due to inertia, the firebrands with density of 70 kg/m^3 released from a height of 40 m, travelled the longest distance approximately 275 m, while the firebrand with the highest density released from a height of 20 m, travelled the least distance which is approximately 75 m. Although, firebrands were released with zero initial velocities, all firebrands accelerated rapidly and attained velocities close to the free stream velocity within approximately 1 s and all firebrands attained their terminal velocity at the time of deposition. The spatial distribution of firebrands which is mainly understood in terms of statistical quantities such as dispersion and diffusivity was also studied. For firebrands released at the height of 40 m, the dispersion remained close to zero until the firebrands encountered the turbulent boundary layer after which the dispersion increased significantly. Normalized statistics pertaining to the distribution of landed firebrands was also calculated. Statistics pertaining to the coordinates of the landed firebrands in the streamwise and spanwise directions were calculated. In all simulated cases, the streamwise variance was found sub-

stantially larger than the spanwise variance. The co-variance was found negligible. After calculation of skewness and kurtosis, deviation from Gaussianity was found significant in the cases where the density of firebrands was 230 and 570 kg/m^3 and the release height was from 40 m. The statistical techniques that are introduced in this work to characterize the moving and deposited firebrands can have applications in situations where flow configuration is different from what is considered in this work.

References

Albini, F., 1983. Transport of firebrands by line thermals. Combust. Sci. Technol. 32 (5–6), 277–288.

Albini, F.A., 1979. Spot Fire Distance from Burning Trees. General Technical Report. Intermountain Forest and Range Experiment Station, Missoula, MT.

Anthenien, R.A., Stephen, D.T., Fernandez-Pello, A.C., 2006. On the trajectories of embers initially elevated or lofted by small scale ground fire plumes in high winds. Fire Saf. J. 41 (5), 349–363.

Armenio, V., Fiorotto, V., 2001. The importance of the forces acting on particles in turbulent flows. Phys. Fluids 13 (8), 2437–2440.

Böning, C.W., 1988. Characteristics of particle dispersion in the north atlantic: an alternative interpretation of sofar float results. Deep Sea Res. Part A. Oceanogr. Res. Papers 35 (8), 1379–1385.

Chernogorova, T., Vulkov, L., 2014. A finite volume difference scheme for a model of settling particle dispersion from an elevated source in an open-channel flow. Comput. Math. Appl. 67 (12), 2099–2111.

Coles, D., 1956. The law of the wake in the turbulent boundary layer. J. Fluid Mech. 1 (2), 191–226.

Crowe, C.T., Schwarzkopf, J.D., Sommerfeld, M., Tsuji, Y., 2011. Multiphase Flows with Droplets and Particles. CRC Press.

Csanady, G., 1963. Turbulent diffusion of heavy particles in the atmosphere. J. Atmos. Sci. 20 (3), 201–208.

De Graaff, D.B., Eaton, J.K., 2000. Reynolds-number scaling of the flat-plate turbulent boundary layer. J. Fluid Mech. 422, 319–346.

Fernandez-Pello, A.C., 2017. Wildland fire spot ignition by sparks and firebrands. Fire Saf. J. 91, 2–10.

Fryer, G., Johnson, E., 1988. Reconstructing fire behaviour and effects in a subalpine forest. J. Appl. Ecol. 1063–1072.

Goldstein, H., 2011. Classical Mechanics. Pearson Education India.

Himoto, K., Tanaka, T., 2005. Transport of disk-shaped firebrands in a turbulent boundary layer. Fire Saf. Sci. 8, 433–444.

Hoerner, S.F., 1965. Fluid-Dynamic Drag: Practical Information on Aerodynamic Drag and Hydrodynamic Resistance. Hoerner Fluid Dynamics.

Huang, H., Ooka, R., Kato, S., Hayashi, Y., 2007. A numerical study of firebrands scattering in urban fire based on CFD and firebrands aerodynamics measurements. J. Fire Sci. 25 (4), 355–378.

Inoue, M., Pullin, D., 2011. Large-eddy simulation of the zero-pressure-gradient turbulent boundary layer up to Re$_\theta$ = O (10^{12}). J. Fluid Mech. 686, 507–533.

Kaftori, D., Hetsroni, G., Banerjee, S., 1995. Particle behavior in the turbulent boundary layer. II. Velocity and distribution profiles. Phys. Fluids 7 (5), 1107–1121.

Kaimal, J.C., Finnigan, J.J., 1994. Atmospheric Boundary Layer Flows: Their Structure and Measurement. Oxford University Press.

Kelbaliyev, G., 2011. Drag coefficients of variously shaped solid particles, drops, and bubbles. Theor. Found. Chem. Eng. 45 (3), 248–266.

Koo, E., Linn, R.R., Pagni, P.J., Edminster, C.B., 2012. Modelling firebrand transport in wildfires using HIGRAD/FIRETEC. Int. J. Wildland Fire 21 (4), 396–417.

Koo, E., Pagni, P.J., Weise, D.R., Woycheese, J.P., 2010. Firebrands and spotting ignition in large-scale fires. Int. J. Wildland Fire 19 (7), 818–843.

Lund, T.S., Wu, X., Squires, K.D., 1998. Generation of turbulent inflow data for spatially-developing boundary layer simulations. J. Comput. Phys. 140 (2), 233–258.

Mahalingam, S., Cantwell, B., Ferziger, J., 1990. Full numerical simulation of coflowing, axisymmetric jet diffusion flames. Phys. Fluids A 2 (5), 720–728.

Manzello, S.L., Cleary, T.G., Shields, J.R., Maranghides, A., Mell, W., Yang, J.C., 2008. Experimental investigation of firebrands: generation and ignition of fuel beds. Fire Saf. J. 43 (3), 226–233.

Manzello, S.L., Maranghides, A., Mell, W.E., 2007. Firebrand generation from burning vegetation. Int. J. Wildland Fire 16 (4), 458–462.

Manzello, S.L., Maranghides, A., Shields, J.R., Mell, W.E., Hayashi, Y., Nii, D., 2009. Mass and size distribution of firebrands generated from burning Korean pine (Pinus koraiensis) trees. Fire Mater. 33 (1), 21–31.

Maranghides, A., Mell, W., 2011. A case study of a community affected by the witch and guejito wildland fires. Fire Technol. 47 (2), 379–420.

Marchildon, E., Clamen, A., Gauvin, W., 1964. Drag and oscillatory motion of freely falling cylindrical particles. Can. J. Chem. Eng. 42 (4), 178–182.

Mardia, K.V., 1970. Measures of multivariate skewness and kurtosis with applications. Biometrika 57 (3), 519–530.

Mardia, K.V., 1974. Applications of some measures of multivariate skewness and kurtosis in testing normality and robustness studies. Sankhy 115–128.

Maxey, M., 1987. The gravitational settling of aerosol particles in homogeneous turbulence and random flow fields. J. Fluid Mech. 174, 441–465.

McGrattan, K., Hostikka, S., McDermott, R., Floyd, J., Weinschenk, C., Overholt, K., 2013. Fire Dynamics Simulator Technical Reference Guide volume 1: Mathematical Model, 1018(1). NIST Special Publication, p. 175.

Mell, W., Maranghides, A., McDermott, R., Manzello, S.L., 2009. Numerical simulation and experiments of burning douglas fir trees. Combust. Flame 156 (10), 2023–2041.

Mortensen, P., Andersson, H., Gillissen, J., Boersma, B., 2007. Particle spin in a turbulent shear flow. Phys. Fluids 19 (7), 078109.

Njobuenwu, D.O., Fairweather, M., 2016. Simulation of inertial fibre orientation in turbulent flow. Phys. Fluids 28 (6), 063307.

Oliveira, L.A., Lopes, A.G., Baliga, B.R., Almeida, M., Viegas, D.X., 2014. Numerical prediction of size, mass, temperature and trajectory of cylindrical wind-driven firebrands. Int. J. Wildland Fire 23 (5), 698–708.

Orlanski, I., 1976. A simple boundary condition for unbounded hyperbolic flows. J. Comput. Phys. 21 (3), 251–269.

Pagni, P.J., 1993. Causes of the 20 October 1991 Oakland hills conflagration. Fire Saf. J. 21 (4), 331–339.

Pereira, J.C., Pereira, J., Leite, A.L., Albuquerque, D., 2015. Calculation of spotting particles maximum distance in idealised forest fire scenarios. J. Combust. 2015.

Pitton, E., Marchioli, C., Lavezzo, V., Soldati, A., Toschi, F., 2012. Anisotropy in pair dispersion of inertial particles in turbulent channel flow. Phys. Fluids 24 (7), 073305.

Press, W.H., 1992. The Art of Scientific Computing. Cambridge University Press.

Rai, M.M., Moin, P., 1993. Direct numerical simulation of transition and turbulence in a spatially evolving boundary layer. J. Comput. Phys. 109 (2), 169–192.

Reyes, G., Brown, S., Chapman, J., Lugo, A.E., 1992. Wood densities of tropical tree species. Gen. Tech. Rep. SO-88. New Orleans, LA: US Dept of Agriculture, Forest Service, Southern Forest Experiment Station.

Rogers, C., Eaton, J., 1991. The effect of small particles on fluid turbulence in a flat–plate, turbulent boundary layer in air. Phys. Fluids A 3 (5), 928–937.

Sardina, G., Picano, F., Schlatter, P., Brandt, L., Casciola, C.M., 2014. Statistics of particle accumulation in spatially developing turbulent boundary layers. Flow Turbul. Combust. 92 (1–2), 27–40.

Sardina, G., Schlatter, P., Picano, F., Casciola, C., Brandt, L., Henningson, D.S., 2012. Self-similar transport of inertial particles in a turbulent boundary layer. J. Fluid Mech. 706, 584–596.

Sardoy, N., Consalvi, J., Kaiss, A., Fernandez-Pello, A., Porterie, B., 2008. Numerical study of ground-level distribution of firebrands generated by line fires. Combust. Flame 154 (3), 478–488.

Sardoy, N., Consalvi, J.-L., Porterie, B., Fernandez-Pello, A.C., 2007. Modeling transport and combustion of firebrands from burning trees. Combust. Flame 150 (3), 151–169.

Shotorban, B., Mashayek, F., 2005. Modeling subgrid-scale effects on particles by approximate deconvolution. Phys. Fluids 17 (8), 081701.

Shotorban, B., Mashayek, F., 2006. A stochastic model for particle motion in large-eddy simulation. J. Turbul. (7) N18.

Snyder, W.H., Lumley, J., 1971. Some measurements of particle velocity autocorrelation functions in a turbulent flow. J. Fluid Mech. 48 (1), 41–71.

Spalart, P.R., 1988. Direct simulation of a turbulent boundary layer up to $Re_\theta = 1410$. J. Fluid Mech. 187, 61–98.

Spalding, D., 1961. A single formula for the ælaw of the wallg. J. Appl. Mech. 28 (3), 455–458.

Stephen, D.T., Fernandez-Pello, A.C., 1998. On the flight paths of metal particles and embers generated by power lines in high winds-a potential source of wildland fires. Fire Saf. J. 30 (4), 333–356.

Tarifa, C.S., del Notario, P.P., Moreno, F.G., 1965. On the flight paths and lifetimes of burning particles of wood. In: Symposium (International) on Combustion, vol. 10. Elsevier, pp. 1021–1037.

Taylor, G.I., 1922. Diffusion by continuous movements. Proc. Lond. Math. Soc. 2 (1), 196–212.

Thurston, W., Kepert, J.D., Tory, K.J., Fawcett, R.J., 2017. The contribution of turbulent plume dynamics to long-range spotting. Int. J. Wildland Fire 26 (4), 317–330.

Tohidi, A., Kaye, N.B., 2017. Comprehensive wind tunnel experiments of lofting and downwind transport of non-combusting rod-like model firebrands during firebrand shower scenarios. Fire Saf. J. 90, 95–111.

Tohidi, A., Kaye, N.B., 2017. Stochastic modeling of firebrand shower scenarios. Fire Saf. J. 91, 91–102.

Voth, G.A., Soldati, A., 2017. Anisotropic particles in turbulence. Annu. Rev. Fluid Mech. 49, 249–276.

Werner, H., Wengle, H., 1993. Large-Eddy simulation of turbulent flow over and around a cube in a plate channel. In: Turbulent Shear Flows 8. Springer, pp. 155–168.

Wilson, R., Brown, M., 1977. Variation in Char Density on Laboratory Fuels [Free-burning wood fuels, Pinus Ponderosa, Betula]. General Technical Report. Research Note INT-US Dept. of Agriculture, Ogden, UT.

Wu, X., Moin, P., 2009. Direct numerical simulation of turbulence in a nominally zero-pressure-gradient flat-plate boundary layer. J. Fluid Mech. 630, 5–41.

Yin, C., Rosendahl, L., Kær, S.K., Sørensen, H., 2003. Modelling the motion of cylindrical particles in a nonuniform flow. Chem. Eng. Sci. 58 (15), 3489–3498.

Yin, C., Rosendahl, L., Kær, S.K., Sørensen, H., 2011. Corrigendum to ®modelling the motion of cylindrical particles in a nonuniform flowg[chemical engineering science 58 (2003) 3489–3498]. Chem. Eng. Sci. 66 (1), 117.